Mid-infrared upconversion based hyperspectral imaging

Junaid, Saher; Tomko, Jan; Semtsiv, Mykhaylo P.; Kischkat, Jan; Masselink, W. Ted; Pedersen, Christian; Tidemand-Lichtenberg, Peter

Published in:
Optics Express

Link to article, DOI:
10.1364/OE.26.002203

Publication date:
2018

Document Version
Publisher's PDF, also known as Version of record

Research Article | Vol. 26, No. 3 | 5 Feb 2018 | OPTICS EXPRESS 2203
Optics EXPRESS

Mid-infrared upconversion based hyperspectral imaging

SAHER JUNAID,[1,*] JAN TOMKO,[2] MYKHAYLO P. SEMTSIV,[2] JAN KISCHKAT,[2] W. TED MASSELINK,[2] CHRISTIAN PEDERSEN,[1] AND PETER TIDEMAND-LICHTENBERG[1]

[1]*DTU Fotonik, Frederiksborgvej 399, Roskilde 4000, Denmark*
[2]*Humboldt University Berlin, Department of Physics, Newton Street 15, 12489 Berlin, Germany*
**sahju@fotonik.dtu.dk*

Abstract: Mid-infrared hyperspectral imaging has in the past decade emerged as a promising tool for medical diagnostics. In this work, nonlinear frequency upconversion based hyperspectral imaging in the 6 to 8 μm spectral range is presented for the first time, using both broadband globar and narrowband quantum cascade laser illumination. $AgGaS_2$ is used as the nonlinear medium for sum frequency generation using a 1064 nm mixing laser. Angular scanning of the nonlinear crystal provides broad spectral coverage at every spatial position in the image. This study demonstrates the retrieval of series of monochromatic images acquired by a silicon based CCD camera, using both broadband and narrowband illumination and a comparison is made between the two illumination sources for hyperspectral imaging.

OCIS codes: (190.7220) Upconversion; (040.1490) Cameras; (040.3060) Infrared.

References and links

1. B. Van Eerdenbrugh and L. S. Taylor, "Application of mid-IR spectroscopy for the characterization of pharmaceutical systems," Int. J. Pharm. **417**(1-2), 3–16 (2011).
2. H. Amrania, G. Antonacci, C. H. Chan, L. Drummond, W. R. Otto, N. A. Wright, and C. Phillips, "Digistain: a digital staining instrument for histopathology," Opt. Express **20**(7), 7290–7299 (2012).
3. R. Bhargava, "Infrared spectroscopic imaging: the next generation," Appl. Spectrosc. **66**(10), 1091–1120 (2012).
4. D. C. Fernandez, R. Bhargava, S. M. Hewitt, and I. W. Levin, "Infrared spectroscopic imaging for histopathologic recognition," Nat. Biotechnol. **23**(4), 469–474 (2005).
5. A. Travo, O. Piot, R. Wolthuis, C. Gobinet, M. Manfait, J. Bara, M. E. Forgue-Lafitte, and P. Jeannesson, "IR spectral imaging of secreted mucus: a promising new tool for the histopathological recognition of human colonic adenocarcinomas," Histopathology **56**(7), 921–931 (2010).
6. J. Nallala, G. R. Lloyd, M. Hermes, and N. Shepherd, "Enhanced spectral histology in the colon using high-magnification benchtop FTIR imaging," Vib. Spectrosc. **2610**, 83 (2016).
7. F. Penaranda, V. Naranjo, L. Kastl, B. Kemper, G. R. Lloyd, J. Nallala, N. Stone, and J. Schnekenberger, "Multivariate classification of fourier transform infrared hyperspectral images of skin cancer cells," in *proceedings of IEEE European Signal Processing Conference* (IEEE, 2016), pp. 1328–1332.
8. A. Rogalski, "Infrared detectors: an overview," Infrared Phys. Technol. **43**(3-5), 187–210 (2002).
9. J. Midwinter, "Image conversion from 1.6μm to the visible in lithium niobate," Appl. Phys. Lett. **13**(3), 68–70 (1968).
10. L. Huot, P. M. Moselund, P. Tidemand-Lichtenberg, L. Leick, and C. Pedersen, "Upconversion imaging using an all-fiber supercontinuum source," Opt. Lett. **41**(11), 2466–2469 (2016).
11. M. Mathez, P. J. Rodrigo, P. Tidemand-Lichtenberg, and C. Pedersen, "Upconversion imaging using short-wave infrared picosecond pulses," Opt. Lett. **42**(3), 579–582 (2017).
12. J. S. Dam, P. Tidemand-Lichtenberg, and C. Pedersen, "Room-temperature mid-infrared single-photon spectral imaging," Nat. Photonics **6**(11), 788–793 (2012).
13. J. S. Dam, C. Pedersen, and P. Tidemand-Lichtenberg, "Theory for upconversion of incoherent images," Opt. Express **20**(2), 1475–1482 (2012).
14. L. M. Kehlet, P. Tidemand-Lichtenberg, J. S. Dam, and C. Pedersen, "Infrared upconversion hyperspectral imaging," Opt. Lett. **40**(6), 938–941 (2015).
15. H. Maestre, A. J. Torregrosa, and J. Capmany, "IR image upconversion under dual-wavelength laser illumination," IEEE Photonics J. **8**(6), 6901308 (2016).
16. H. Maestre, A. J. Torregrosa, and J. Capmany, "IR Image upconversion using band-limited ASE illumination fiber sources," Opt. Express **24**(8), 8581–8593 (2016).

#315265 https://doi.org/10.1364/OE.26.002203
Journal © 2017 Received 13 Dec 2017; revised 14 Jan 2018; accepted 15 Jan 2018; published 22 Jan 2018

Optics EXPRESS

17. S. Wolf, J. Kiessling, M. Kunz, G. Popko, K. Buse, and F. Kühnemann, "Upconversion-enabled array spectrometer for the mid-infrared, featuring kilohertz spectra acquisition rates," Opt. Express **25**(13), 14504–14515 (2017).
18. P. Tidemand-Lichtenberg, J. S. Dam, H. V. Andersen, L. Høgstedt, and C. Pedersen, "Mid-infrared upconversion spectroscopy," J. Opt. Soc. Am. B **33**(11), D28–D35 (2016).
19. J. Falk and W. B. Tiffany, "Theory of parametric upconversion of thermal images," J. Appl. Phys. **43**(9), 3762–3769 (1972).
20. S. Junaid, P. Tidemand-Lichtenberg, and C. Pedersen, "Upconversion based spectral imaging in 6 to 8μm spectral regime," Proc. SPIE **10088**, 100880I (2017).
21. J. Kischkat, S. Peters, B. Gruska, M. Semtsiv, M. Chashnikova, M. Klinkmüller, O. Fedosenko, S. Machulik, A. Aleksandrova, G. Monastyrskyi, Y. Flores, and W. Ted Masselink, "Mid-infrared optical properties of thin films of aluminum oxide, titanium dioxide, silicon dioxide, aluminum nitride, and silicon nitride," Appl. Opt. **51**(28), 6789–6798 (2012).

1. Introduction

Hyperspectral imaging in the mid-infrared (MIR) range is a promising tool for a wide range of applications in medical diagnostics [1], such as histopathological study of tissue samples employed for cancer diagnostics [2–5]. The traditional approach for MIR hyperspectral imaging is Fourier Transform Infrared Spectroscopy (FTIR) using Focal Plane Array (FPA) detectors [6,7]. However, direct detection in the MIR is limited in terms of sensitivity, cost and complexity [8].

Nonlinear frequency upconversion based MIR detection is emerging as a promising technology for many MIR applications. Upconversion detection has already been employed for both spectroscopy and imaging, used in both pulsed and continuous wave applications. Most work has been based on lithium niobate (LN) as the nonlinear medium, using either bulk [9–11] or periodically poled [12–17] crystals, however, applications of LN is limited by the transparency range of the material. Above 5 μm upconversion spectroscopy [18] and polychromatic imaging [19, 20] has been demonstrated based on Ag_3AsS_3 or $AgGaS_2$.

This work demonstrates, to the best of our knowledge, the first application of upconversion technology for hyperspectral imaging in the 6 to 8 μm range. The setup consists of an upconversion unit based on $AgGaS_2$ (AGS) as the nonlinear material and a 1064 nm mixing laser. A globar i.e. a broadband source and a quantum cascade laser (QCL) i.e. a narrowband source is used for illumination and a comparison is made between the two approaches based on parameters such as spectral resolution and image acquisition speed. A novel technique for hyperspectral imaging exploiting birefringent non-collinear phase matching in the nonlinear crystal is implemented together with post-processing of the acquired images. Scanning of the phase match condition is implemented by rotation of the nonlinear crystal relative to its $\hat{c}$-axis, which enables imaging of every pixel within the field of view with full spectral information encoded. This approach is only viable for imaging when performing the frequency conversion in the Fourier plane of the system (a translation in the Fourier plane coursed by crystal rotation only results in an angle in the image plane, i.e. the camera position). Scanning of the phase match condition for hyperspectral imaging has previously been demonstrated in the 3 μm spectral range by temperature tuning of a periodically poled LN crystal [14], however, leading to a very low image acquisition rate due to a slow thermal tuning rate, as well as power instabilities due to the intra-cavity nature of that system.

The imaging setup is presented in the first section of the paper. In the following sections, the image acquisition and monochromatic image post-processing algorithm is demonstrated, first based on globar and then for QCL illumination. Finally, the spectral and spatial resolution is evaluated for the two cases and a comparison between their performances is made.

Optics EXPRESS

2. Setup and image acquisition

In this study, a MIR hyperspectral imaging system is demonstrated based on nonlinear frequency upconversion. An $AgGaS_2$ (AGS) crystal 5x5x10 mm^3, cut at 48° (with respect to $\hat{c}$-axis) is used as the nonlinear medium for Sum Frequency Generation (SFG) of the MIR signal and the mixing field. First a globar and then a QCL is used as MIR illumination sources whereas a diode pumped Nd:YVO_4 continuous wave (CW) 1064 nm laser delivering up to 1.7 W of power in a fundamental Gaussian mode is used as the mixing field. A detailed description of the upconversion unit can be found in [20], Junaid, et al. Non-collinear birefringent phase matching is exploited; by rotation of the nonlinear crystal the phase match condition is scanned enabling broad spectral coverage over the full field of view. The theory of non-collinear birefringent phase matching in AGS is explained in detail in [18], T. Lichtenberg, et al.

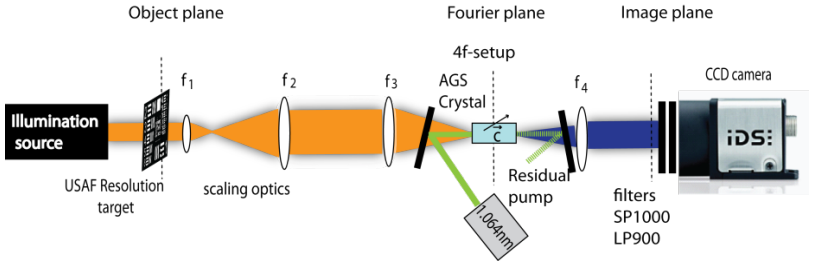

Fig. 1. Single-pass upconversion system using globar/QCL as illumination sources and a 1064 nm laser as mixing field for sum frequency generation. Zinc Selenide ($ZnSe_2$) lenses are used for the MIR signal, where f_1 and f_2 can be applied for object magnification, f_3 (= 50 mm) is used to focus the object light into the nonlinear crystal for non-collinear upconversion and provides with f_4 (= 60 mm) a 4f-imaging system with the nonlinear conversion occurring in the Fourier plane. Filters (short pass 1000, long pass 900) and a mirror is used to eliminate the residual pump and stray light from the upconverted signal. An IDS Silicon camera is used for the image acquisition. A clear optical path USAF resolution target and/or polystyrene film (not shown) is used as an object.

Figure 1 shows the imaging system including an illumination source and the upconversion detection system. A USAF resolution target is illuminated by the MIR light source which is then magnified using a pair of lens (f_1 and f_2) by the factor of f_2/ f_1. The beam is then focused into the nonlinear crystal using lens f_3 for non-collinear phase matching with the 1064 nm mixing laser field with a beam diameter of ~1 mm ($1/e^2$ diameter of the Gaussian beam). f_4 forms together with f_3 a 4f-imaging system between the object plane and image plane, where an IDS 1.31 Mpixel CCD camera is used for upconverted image acquisition. A pair of filters and a mirror is used to block stray light and residual mixing signal.

2.1 Globar illumination

In this section the images acquired with the globar illumination i.e. a broadband source, is presented. A USAF resolution target (clear optical path, Edmund optics) is used as a test sample carrying well-defined spatial features to assess the spatial resolution of the imaging system. Furthermore, a polystyrene film (PS) is used, either alone or in combination with the resolution target to impose spectral features. The scaling optics is used to resolve smaller spatial features of the sample, however, at the expense of a reduced field of view.

Figure 2 shows upconverted images acquired with the Si CCD camera for a crystal rotation of 3°, increasing crystal rotation means decreasing collinear angle relative to the crystal $\hat{c}$-axis. Figure 2(a) shows an upconverted image of the illumination source alone (without any target), demonstrating the field of view of the imaging system as well as the spatial and spectral homogeneity of the illumination source. In Fig. 2(b) a PS film is introduced in the object plane, where the dark ring corresponds to the PS absorption line at

Optics EXPRESS

6.7 µm. Figure 2(c) depicts an acquired image combining resolution target and PS film, note the field of view is limited by the resolution target. The smallest resolvable element in this image is group 0, element 6 corresponding to approx. 280 µm. Finally, Fig. 2(d) shows the upconverted image of the resolution target with a magnification of 6.667 (f_2/ f_1 = 100/15) resolving the smallest features of the target (Group 3, element 6) i.e. 35µm.

The radial wavelength dependence in the upconverted image is dictated by the non-collinear phase match condition of the upconversion process in the Fourier space [19]. A series of images is captured while rotating the nonlinear crystal where the spectral features of PS can be observed in the 6 to 8 µm range (Visualization 1). A second series of images is taken while rotating the crystal including both PS film and resolution target (Visualization 2).

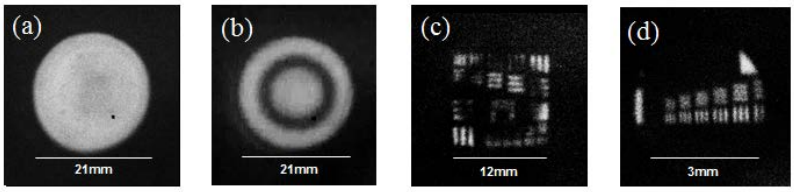

Fig. 2. Upconverted images at 3° crystal rotation (with respect to $\hat{c}$-axis) using 500 ms camera integration time (the scale bar refers to the object plane (a) Upconverted image without any sample with full field of view, (b) with PS film showing the absorption line at 6.7 µm. (c) Upconverted images of USAF resolution target and PS film, (d) magnification of 6.667 (100/15) is applied to resolve the smallest features of the resolution target i.e. 35 µm.

The number of spatially resolvable elements is estimated as the ratio of total area (field of view) over the smallest resolvable element, $\pi(10.5\text{ mm})^2/(0.280\text{ mm})^2$ (in the object plane). Approx. 4400 is achieved in this study independent of the scaling optics. The signal to background ratio of the image acquisition can be estimated by the ratio of the camera integration time for the upconverted images relative to the integration time for equivalent intensity of the background i.e. 0.3s/2s. Here 0.3s is used for signal acquisition instead of 0.5s used in Fig. 2, because the maximum integration time of the camera is 2s which was not sufficient for similar intensity of the background compared to signal intensity therefore integration time of 0.3s is used for signal.

In the following the post-processing of the acquired upconverted images in order to extract monochromatic images is explained. In this approach, the acquired images are simply convolved with a response function for the specific wavelength (and crystal orientation) and summed. To construct monochromatic images, the spatial information, at the wavelength of interest, is extracted from each upconverted image for all crystal rotation angles calculated from the phase match condition. This is obtained from pixel wise multiplication of the acquired upconverted images and a numerically calculated spectral image response function for the specific rotation angle of the nonlinear crystal at the wavelength of interest. These predominantly circular single-wavelength intensity distributions (corresponding to the different crystal rotation angles) are then summed to form monochromatic images with full field of view. An automated MatLab program is developed for the post-processing of series of upconverted images, captured as a function of the rotation angle of the nonlinear crystal.

The monochromatic image acquisition algorithm can be represented as

$$\left\{\begin{matrix}\text{Upconverted image intensity}\\ \text{at crystal rotation angle } \theta_i\end{matrix}\right\} = I_{up}(\theta_i), \quad (1)$$

$$\left\{\begin{matrix}\text{Numerical single-wavelength image response}\\ \text{function at crystal rotation angle } \theta_i\end{matrix}\right\} = R_{\lambda}(\theta_i), \quad (2)$$

Optics EXPRESS

$$I_{mono}(\theta_i) = I_{up}(\theta_i) \times R_\lambda(\theta_i), \quad (3)$$

where "×" symbolize a pixel by pixel multiplication of the upconverted intensity $I_{up}(\theta_i)$ and the normalized phase matched wavelength response in the image $R_\lambda(\theta_i)$, giving the monochromatic image at wavelength λ at crystal rotation angle θ_i. This step represents the extraction of single-wavelengths from the polychromatic upvconverted images. This procedure is repeated for all crystal rotation angles and the full monochromatic image is obtained as the sum of these individual contributions

$$I_{mono} = \sum_{i=0}^{n} I_{mono}(\theta_i). \quad (4)$$

I_{mono} represents the monochromatic image at full field of view, when the crystal is rotated in n steps, from 0 to θ_{max} degree. This procedure is repeated for the full spectral range of interest resulting in series of monochromatic images forming the hyperspectral image cube. To obtain high quality monochromatic images in terms of spatial and spectral information, the angular step size of the crystal rotation angle should be kept small enough to reduce the intensity variations within the reconstructed images. This is illustrated in Fig. 3, however, normalization of the summed images can be done to allow for lower sampling of the crystal rotation angle. Figure 3(a) illustrates the simulated $Sinc^2$ - function intensity distributions as a function of non-collinear mixing angles at 6.9 µm while the crystal is rotated from 0° to 10° in steps of 0.5°. The dashed line shows the homogeneous intensity profile obtained by summing the narrowband $Sinc^2$ - functions. This can potentially be used for normalization of the monochromatic images. Figure 3(b) represents the 2D response function for the monochromatic image acquisition algorithm (described as $R_\lambda(\theta_i)$ in Eq. (2)), when $\lambda = 6\,\mu m$ and crystal rotation angle is set to 10^o.

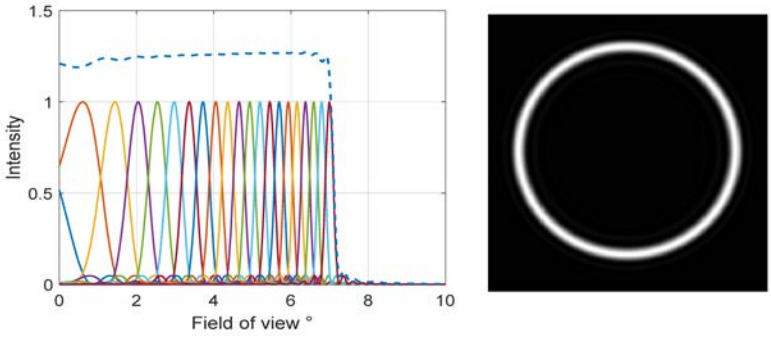

Fig. 3. (a) Simulated $Sinc^2$ - function intensity distribution at 6.9 µm while rotating the crystal from 0° to 10° in steps of 0.5°. Dashed line shows the summation of all the intensity distribution within the full field of view, (b) 2D response function used for monochromatic image acquisition algorithm,, at wavelength 6 µm and crystal rotation angle 10°.

Figure 4 shows two monochromatic images acquired by post-processing of a series of upconverted images of a broadband illuminated USAF resolution target including the PS film as shown in Fig. 2(c). The series of images is acquired while rotating the crystal from 0 to 20° in steps of 0.5°. Figures 4(a) and 4(b) show reconstructed monochromatic image of the target at 6.5 µm and 6.7 µm, respectively. Comparing the two images the absorption line of PS at 6.7 µm can be noticed from the decreased intensity contrast. A series of monochromatic images is computed in the 6 to 7 µm spectral range where the PS spectral absorption features are evident. This can be seen as intensity variations in the monochromatic images

Optics EXPRESS

(Visualization 3). In Visualization 3, size scaling of the monochromatic images can be observed depending on the wavelength, dictated by the scaling factor related to the transverse phase matching equation [17].

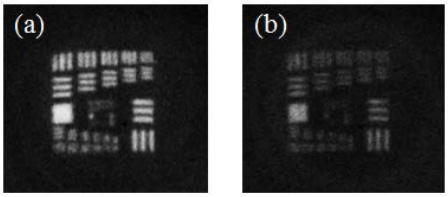

Fig. 4. Monochromatic images of USAF resolution target combined with PS film containing both spatial and spectral features acquired by upconversion and post-processing of broadband illuminated target. (a) at 6.5 µm and (b) 6.7 µm wavelength.

The spectral bandwidth of the upconversion process is dependent on the center wavelength, and the incoming MIR angle, which is conserved in the post-processing step, hence, the spectral bandwidth in the monochromatic image increase slightly radially in the image. Thus, the spectral resolution deteriorates with increasing MIR angles as depicted in [18], T. Lichtenberg, et al, Fig. 5.

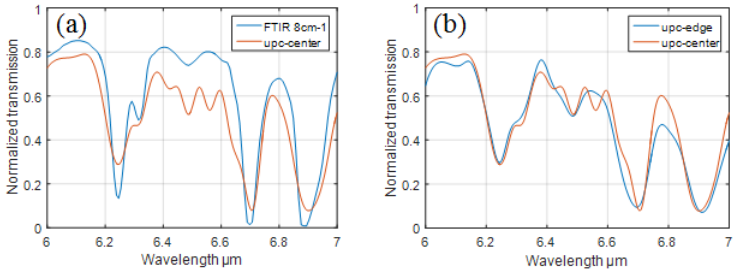

Fig. 5. Measured transmission spectra of polystyrene (a) comparing the FTIR measurement with the upconversion (b) comparison of the spectral resolution depending on the position of the images based on upconversion. It can be noticed that the spectral resolution deteriorates along radial direction

Figure 5 shows the measured spectrum of PS film based on FTIR and upconversion. The spectrum measured with FTIR is recorded at 8 cm^{-1} spectral resolution. Two curves are plotted using upconversion, one based on the central pixel of the images (upc-center) and the other is taken when pixels on the edge of the field of view are considered (upc-edge). It is noted that the spectral resolution for upc-edge is worse than that of the upc-center as seen from Fig. 3(b).

2.2 QCL illumination

In this section, upconversion based spectral images are presented using a narrow band tunable QCL as the illumination source.

The QCL used in this experiment is operated in an external cavity configuration with a tunable diffraction grating enabling selection of the desired wavelength. A Littrow configuration with back facet output-coupling is used to achieve higher average power, however scarifying some tunability. The working principle relies on electrical pumping of the QCL crystal. A portion of the amplified light is emitted through an antireflection (AR) coated ($\lambda/4$ of Y_2O_3) intra-cavity facet onto a diffraction grating. The minus first diffraction order is used to select the desired wavelength and is retro-reflected into the QCL crystal for further amplification. Tunability of the laser is given by the gain spectrum of the active region, design and available materials [21] for the AR coating on the intra-cavity facet and the overall

Optics EXPRESS

back coupling efficiency from the diffraction grating. The utilized tuning range covered here is from 5.9 to 6.19 µm with a measured linewidth below 4 nm. Average power at 6 µm is 4.5 mW, with a pulse repetition rate of 0.5 MHz and a pulse duration of 50 ns, leading to duty cycle of 2.5%.

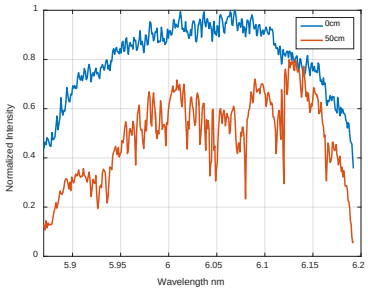

Fig. 6. Spectral tuning range of QCL measured with cooled MCT detector at 0 and 50 cm distance away from the laser cavity window. Water absorption lines can be noted in the red curve which corresponds to 50 cm distance from the laser cavity window.

A USAF resolution target is illuminated by a QCL beam of ~1.2 mm diameter which is then magnified using a pair of lens (f_1 and f_2) by a factor of 18.75 ($f_2/ f_1 = 75/4$) (see Fig. 6). The beam is then focused into the nonlinear crystal using lens f_3 for mixing with the 1064 nm laser field. By employing both crystal angle tuning and QCL wavelength tuning, a series of monochromatic images i.e. a hyperspectral cube is achieved.

In case of QCL illumination, the monochromatic image acquisition algorithm is straight forward compared to that of the globar illumination. In present case no deconvolution is required, monochromatic images are obtained just by summing the images obtained while rotating the nonlinear crystal. This process is repeated for every QCL wavelength of interest.

$$I_{\lambda} = \sum_{i=0}^{n} I_{up}(\theta_i) \tag{5}$$

$$I_{hsp} = I_{\lambda_1}, I_{\lambda_2} \ldots I_{\lambda_m}. \tag{6}$$

where $I_{up}(\theta_i)$ represents the upconverted image as a function of crystal rotation angle, ranging from 0 to n, I_{λ} represents a monochromatic image at wavelength λ and I_{hsp} represents a series of monochromatic images from wavelength λ_1 to λ_m.

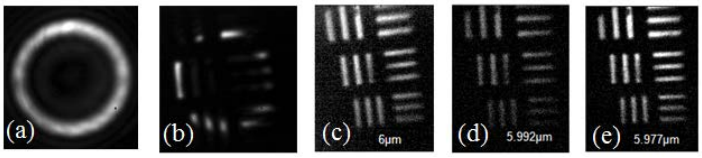

Fig. 7. Upconverted images (a) at 6 µm with magnification (18.75 times), with crystal rotated at 11.05 ° with camera integration time 10 ms, 1.5 W of pump power (b) with resolution target (c, e) Monochromatic (post processed) image of the smallest spatial features (14.25 lines/mm) of USAF resolution target at off resonance, and (d) on resonance of water absorption line.

Figure 7(a) and 7(b) depict an upconverted image with a magnification factor of 18.75 (f_2/ f_1) without sample and with USAF resolution target as a sample, respectively. The crystal is rotated to 11.05° and the pump power is set to approx. 1.5 W. A Visualization 4 has been made which depicts the effect of rotating the nonlinear crystal with respect to the $\hat{c}$-axis when the QCL wavelength was fixed at 6 µm. The crystal was rotated from 9.7° to 12.6° to cover the full field of view. Figures 7(c)-7(e) show the smallest features of the USAF resolution

target (14.25 lines/mm i.e. 35.08 µm smallest resolvable element) including spectral water absorption features. The three images are taken ON and OFF resonance of a water absorption line which can be seen from the intensity difference. The measurement is taken by simply utilizing the water content in the air with a path length of approx. 50 cm. The humidity in the laboratory was measured to be 32% at 22.6° C temperature. Visualization 5 demonstrates series of upconverted images while tuning the QCL from 6.19 µm to 6 µm at fixed crystal rotation angle, i.e. 9.752°.

3. Comparison

In this work, two different illumination sources are investigated using the same upconversion module and a comparison is made highlighting different aspects of the two approaches. The Globar, due to its low intensity, offers slow acquisition of images. Using the same upconversion module with a globar as an illumination source, the integration time of the camera was set to 500 ms whereas using a QCL leads to 50 times faster image acquisition per frame i.e. 10 ms. However the globar, being a broadband source has the advantage of faster acquisition of a whole set of data by a single sweep of crystal rotation angle, whereas, in case of a QCL the process has to be repeated for every wavelength.

The monochromatic image acquisition algorithm is more straight forward in case of narrowband illumination, compared to broadband sources where the deconvolution of every wavelength contribution is acquired based on the phase matching condition, before summing up the individual wavelength contributions to form a monochromatic image.

Using a narrowband illumination source for upconversion based hyperspectral imaging has the advantage of a constant spectral resolution of the image dictated by the linewidth of the source itself whereas in case of a broadband source, the spectral resolution is set by the acceptance bandwidth of the upconversion device which even varies radially within a single image.

The spatial resolution remains the same in case of both illumination sources. In case of coherent illumination sources, there will be a factor of $\sqrt{2}$ decrement in spatial resolution, which has been demonstrated already in [13]. Also spatial resolution of the system doesn't change with magnification, i.e. number of resolvable pixel elements remains the same regardless of the magnification.

4. Summary

This paper is, to the best of our knowledge, the first demonstration of mid-infrared hyperspectral imaging based on upconversion technology in 6 to 8 µm spectral range. In this work $AgGaS_2$ is used as the nonlinear medium. Two kinds of MIR illumination sources are used: a standard globar as a source of low-intensity broadband illumination and a QCL as a tunable source of high-intensity, narrow-band illumination. The illumination source is mixed with a 1064 nm solid state laser for upconversion based hyperspectral imaging. The system is compared for the two different illumination sources, assessed primarily by acquisition time and spectral resolution. A series of upconverted images is captured with a Silicon CCD camera while scanning the phase match condition, i.e. rotation of the nonlinear crystal, which leads to fast acquisition of images containing radially, distributed spectral information. No translation of the images was observed which shows that the upconversion is performed in the Fourier plane. A MatLab program is used for post-processing of the images to construct monochromatic images based on the scanning of the phase match condition.

A USAF resolution target is used as a sample and the smallest features of the target (14.25 lines/mm) have been resolved by applying magnification on the object (MIR) side. Water and polystyrene absorption lines have been used as spectral features in conjunction with the USAF resolution target. The imaging system can, in the implemented configuration resolve up to 4400 spatial elements within the field of view, which can be improved further by

Optics EXPRESS

increasing the beam diameter of the mixing laser, however, at the expense of decreased intensity.

Funding

Mid-TECH H2020-MSCA-ITN-2014 (642661).

Acknowledgment:

The authors also thank prof. Nick Stone, Exeter University, for his insightful discussion about biomedical applications of MIR imaging.